applied sciences

MDPI

Article

Mechanical Behavior and Failure of Pre-Existing Crack Rock Under Compression and Creep: Experimental and Numerical Insights

Yang Yuan [1], Teng-Fei Fu [2], Tian-Tian Chen [3,*], Shuo-Nan Zhang [4] and Lian-Ku Xie [1]

[1] Information Institute, Ministry of Emergency Management of the PRC, Beijing 100029, China
[2] School of Electric Power, Civil Engineering and Architecture, Shanxi University, Taiyuan 030024, China
[3] State Key Laboratory of Coastal and Offshore Engineering, Dalian University of Technology, Dalian 116024, China
[4] National Earthquake Response Support Service, Beijing 100049, China; zhangshuonan123@gmail.com
* Correspondence: chentiantian0304@163.com

Abstract

Understanding the mechanical behavior of pre-cracked rock masses is essential for assessing geohazards in deep mining. This study combines laboratory experiments and numerical modeling to investigate the effects of double-crack inclination angles on the strength, crack evolution, and creep behavior of sandstone. Uniaxial compression and multi-stage creep tests were conducted on red sandstone specimens with a fixed crack 1 (60°) and a crack 2 varying from 0° to 150°. A UDEC-Voronoi grain-based model was calibrated against experimental results. The results show that uniaxial compressive strength varies non-linearly with crack angle, reaching a minimum at 30° and a maximum at 90°. Tensile microcracks dominate the failure process (>90%), while shear cracks play a minor role. Under creep loading (70–95% of peak strength), creep lifetime decreases sharply with increasing stress, and microcrack accumulation follows three distinct phases: decelerating, steady-state, and accelerating creep. The numerical model successfully reproduces the observed strength anisotropy, crack patterns, and time-dependent deformation. These findings highlight the critical role of crack inclination in controlling rock mass instability and provide a validated modeling approach for long-term geohazard assessment in fractured rock environments.

Keywords: pre-cracked rock; crack inclination; uniaxial compression; creep; discrete element method

Check for updates

Received: 20 September 2026
Revised: 15 October 2026
Accepted: 15 October 2026
Published: 30 October 2026

Copyright: © 2026 by the authors. Licensee MDPI, Basel, Switzerland. This article is an open access article distributed under the terms and conditions of the Creative Commons Attribution (CC BY) license.

1. Introduction

Diagenetic and tectonic processes lead to a complex distribution of mineral compositions and their spatial arrangement within rocks. Under external loads (e.g., stress, seepage, temperature), microcracks initiate inside the rock. The orientation, size and spatial distribution of these microcracks often exhibit a certain orderliness, which significantly influences the subsequent fracture path and failure mode of the rock [1]. Owing to the direction-dependent nature of crack growth, the mechanical response of the rock also becomes anisotropic [2]. As shallow mineral resources are gradually depleted, mining has shifted to greater depths. Deep mining is typically conducted in a complex geological environment characterized by high in situ stress, high temperature, high pore pressure, and mining-induced disturbance [3–6]. This special condition significantly accelerates the initiation and propagation of fracture networks within the surrounding rock [7–9]. Recent

accident statistics indicate that among dynamic disasters (e.g., rockburst) caused by deep surrounding rock instability, the proportion of fracture-induced accidents has increased. This suggests that internal fractures play a gradually dominant role in the instability process, shifting from stress-dominated to fracture-induced failure. To optimize the prevention and control of instability disasters in deep fractured rock masses, it is necessary to clarify the deformation characteristics and failure mechanisms of fractured rock under load.

Extensive research has been conducted on fractured rock masses through physical experiments and numerical simulations. Laboratory studies have focused on the effects of crack inclination angle, number of cracks and loading rate on strength and crack evolution using digital image correlation (DIC) [10,11] and acoustic emission (AE) [12–14]. For instance, Xu investigated the three-point bending deformation and fracture mechanism of granite with pre-existing cracks [15]. The shear behavior and failure modes of rock masses [16,17] were studied containing Z-shaped and V-shaped intersecting cracks. However, most of these studies focused on single or limited crack geometries, and systematic investigations of double-crack combinations with varying inclinations remain insufficient. Moreover, the time-dependent deformation (creep) behavior of pre-cracked rocks, which is critical for long-term stability assessment, has received less attention.

Numerical methods have become powerful complements to experimental studies. The discrete element method (DEM), in particular, can capture grain-scale interactions such as grain sliding, rolling and bond breakage, which collectively control the macroscopic response of fractured rock [18–20]. Among DEM codes, UDEC with Voronoi tessellation has been shown to realistically represent the meso-structure of sandstone and simulate crack initiation and propagation [21,22]. However, few studies have combined UDEC-Voronoi models with multi-stage creep tests to investigate the time-dependent behavior of pre-cracked rock masses.

This study aims to investigate the effects of double-crack inclination angles on the strength, deformation, crack evolution and creep behavior of sandstone. Laboratory uniaxial compression and multi-stage creep tests were conducted on red sandstone specimens containing a fixed crack 1 (60°) and crack 2 with seven different inclinations (0°, 30°, 60°, 90°, 120°, 150° and intact). DIC and AE were employed to monitor the full-field strain and damage evolution. A 2D Voronoi grain-based discrete element model was then established using UDEC, calibrated against the experimental results, and used to simulate the cracking and creep processes. The validated model provides a tool for assessing long-term geohazards in fractured rock environments.

2. Materials and Methods

2.1. Specimen Preparation

The sandstone used in this study was obtained from in LongChang of Sichuan Province, China, where it is one of the principal surrounding-rock lithologies in deep mining and tunneling. It is a fine-grained, homogeneous red sandstone with few natural discontinuities, which allows the geometry of the artificial flaws to be controlled so that crack inclination is the only dominant variable. Standard cubic specimens of dimensions 50 mm × 50 mm × 100 mm were cut using an infrared cutting machine, and the end surfaces were ground to ensure an unevenness of less than 0.05 mm. Double pre-cracks were fabricated using a high-pressure water jet with a nozzle diameter of 1.5 mm, resulting in a crack thickness of approximately 2.0 mm. The center of crack 1 is 35 mm from the top, and its inclination angle relative to the horizontal remains constant at 60°. The center of crack 2 is 35 mm from the bottom, and its inclination angle varies among 0°, 30°, 60°, 90°, 120°, and 150°. (Figure 1). Intact specimens were also prepared for comparison. The distance

between the two cracks was set to 35 mm from the specimen ends. All specimens were stored in a dry environment before testing.

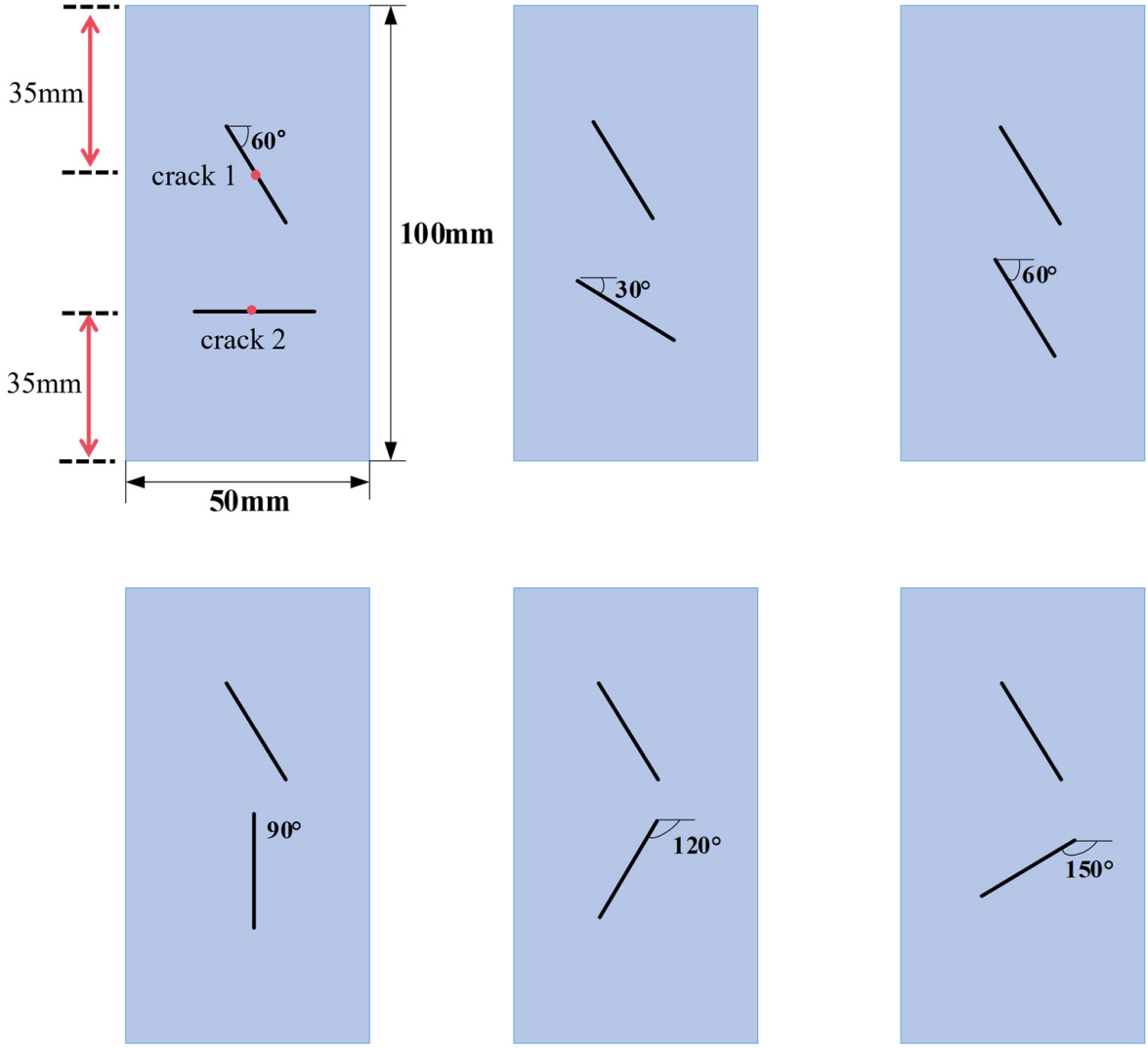


Figure 1. Schematic diagram of double-crack geometry.

2.2. Uniaxial Compression Tests

Uniaxial compression tests were conducted using a WAW-300B servo-controlled electro-hydraulic machine (Jinan Kuangyan Testing Instrument Co., Ltd., Jinan, China) with a maximum load capacity of 300 kN in Figure 2. The loading rate was 0.2 kN/s. During the tests, a DIC system (VIC-2D) was used to capture the full-field strain evolution on the specimen surface. The VIC-2D system provides full-field displacement and strain data for mechanical tests on planar specimens. The technique is based on digital speckle correlation: it measures the true displacement of the object and yields the Lagrangian strain tensor at every point of the object surface. It can measure any in-plane displacement and strain, over a range extending from 50 microstrain to more than 2000%, for objects whose characteristic dimension ranges from 1 mm to 10 m. Its configuration is simple: it requires neither laser light nor special illumination, and only a straightforward calibration procedure together with a random speckle pattern applied to the object under test. An AMSY-6 AE system was employed to record AE ringing counts and energy. The AMSY-6 system acquires several channels in parallel, each with an independently adjustable threshold, sampling rate and pre-amplifier gain, and stores the standard AE parameters (hit count, ringing count, energy,

amplitude, rise time and duration). The AE sensors were attached to the specimen surface using vacuum grease as a couplant and fixed with elastic tape. The two techniques are complementary: DIC provides a continuous, full-field surface displacement/strain map but is insensitive to internal events, whereas AE captures the timing and intensity of internal micro-fracturing but with limited spatial resolution. In this study both systems were started simultaneously from the same external trigger, so that the two data sets share a common time base. The integrated analysis proceeds as follows. (1) The onset of strain localisation (the instant at which a localized high-strain band first appears in the DIC field) is compared with the inflection point of the cumulative AE count/energy; agreement between the two defines the onset of unstable crack growth. (2) The orientation of the DIC localisation band is compared with the AE source-location cloud to verify that macroscopic cracking follows the wing-crack path. (3) The RA–AF characteristics of the AE events are used to classify tensile (low RA, high AF) and shear (high RA, low AF) events; the overwhelming dominance of tensile events is consistent with the numerical prediction that more than 90% of microcracks are tensile.

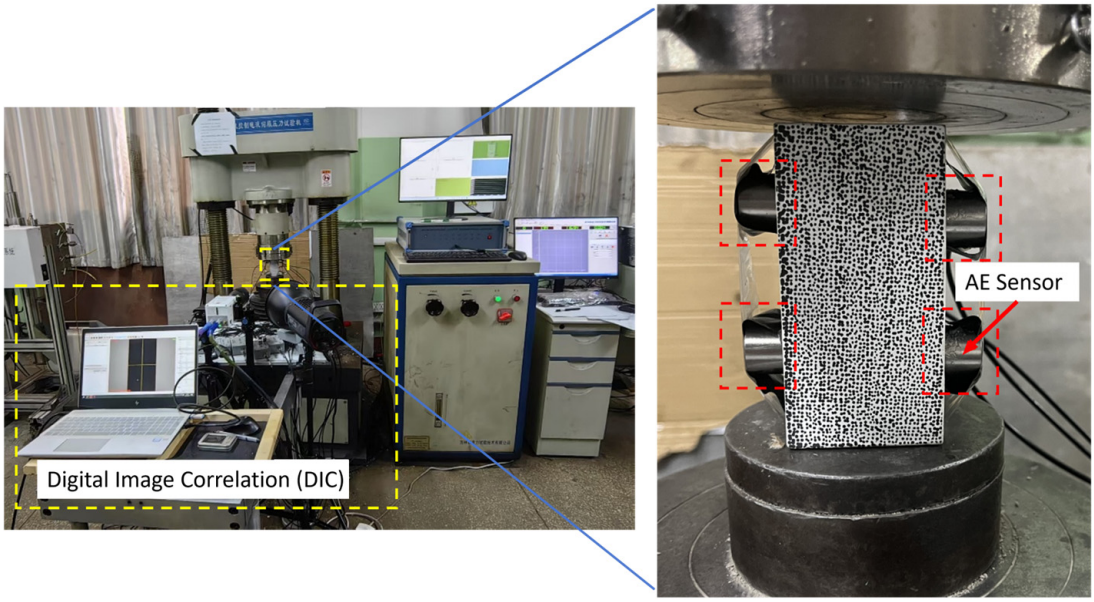


Figure 2. WAW-300B servo-controlled electro-hydraulic machine and sample.

Figure 3 shows the uniaxial compression mechanical behavior of rock specimens with cracks at different inclination angles and the failure process of intact specimens. The intact specimen (Figure 3A) reached a peak strength of 42.4 MPa and failed in a brittle manner. For the double-crack specimens, with crack 1 fixed at 60° and crack 2 varying in angle, the peak strengths were 15.5 MPa (0°), 15.9 MPa (30°), 28.4 MPa (60°), 30.4 MPa (90°), 17.8 MPa (120°) and 26.2 MPa (150°). Accordingly, as the crack 2 angle increases, the uniaxial compressive strength (UCS) follows a non-linear trend: it first decreases to a minimum at 30°, then rises to a maximum at 90°, drops again at 120°, and finally increases slightly at 150° (Figure 3B). DIC analysis revealed that strain localization initially appeared around the tips of the pre-existing cracks. As the axial load increased, wing cracks propagated from the crack tips in the direction of the maximum principal stress. Figure 3C illustrates the failure process of the intact specimen under axial stress. Cracks initiate abruptly at point c, accompanied by stress fluctuations; thereafter, at point d, cracks parallel to the loading direction develop, leading to complete failure.

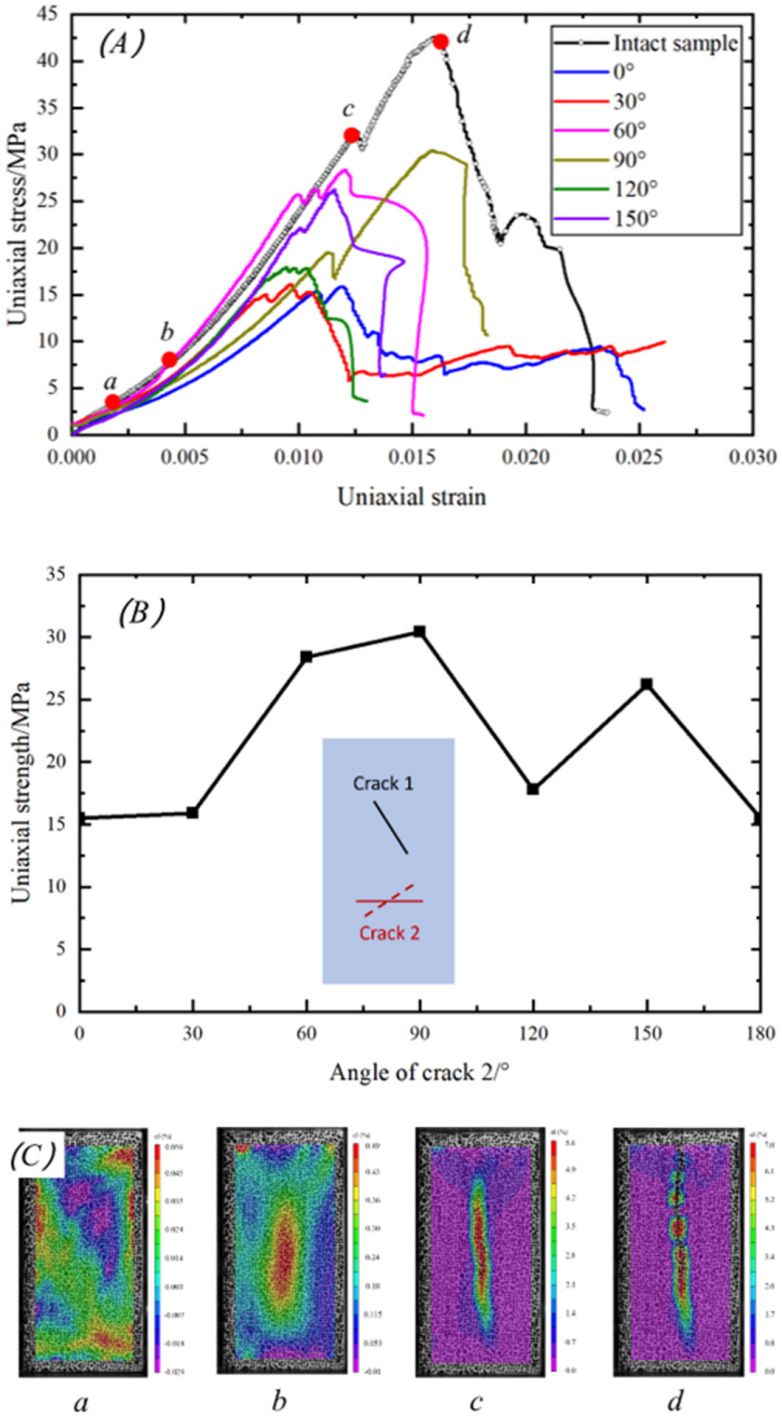


Figure 3. Uniaxial compression mechanical behavior of rock specimens with cracks at different inclination angles and failure process of intact specimens. (**A**) Stress–strain curves under uniaxial compression for specimens with cracks at different inclination angles; (**B**) Uniaxial compressive strength values for specimens with cracks at different inclination angles; (**C**) Failure process of intact rock specimens.

The coalescence of these wing cracks led to the formation of a macroscopic failure surface. For specimens with crack 2 angles of 0° and 30°, the failure was dominated by shear-tensile mixed cracks, while for angles of 60° and 90°, tensile cracks were more prevalent. The final failure patterns of all specimens are shown in Figure 4.

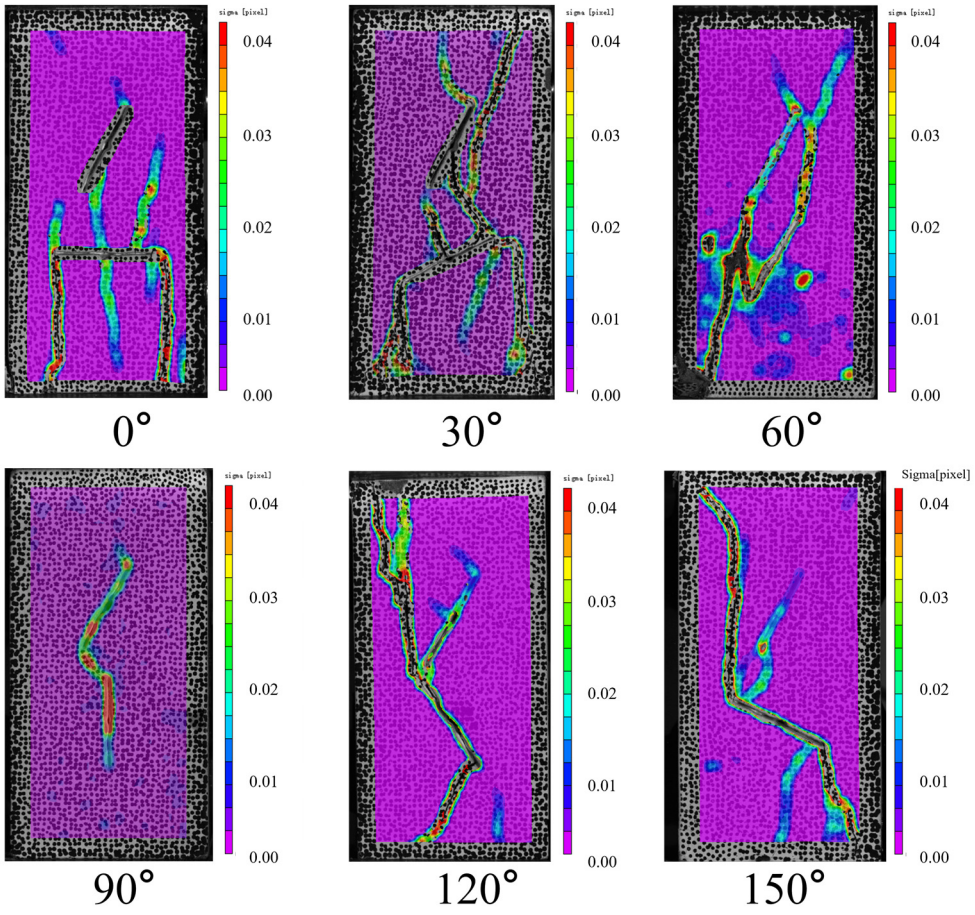


Figure 4. DIC strain field evolution of double-crack specimens.

AE monitoring (Figure 5) showed that the count rate increased slowly during the initial compaction and elastic stages, then surged sharply near the peak stress (black lines). The cumulative AE count (red rectangles) exhibited a clear inflection point at the onset of unstable crack growth. Tensile cracks were found to dominate the AE events, consistent with the DIC observations. The purpose of the cumulative-energy (and cumulative-count) curves is to provide an experimentally measurable proxy for damage accumulation: AE energy is released by microcrack initiation and propagation, so its cumulative value grows in proportion to the number of microcracks and the energy released per event. The curve shape therefore marks the transitions between stable and unstable crack growth.

2.3. Multi-Stage Creep Tests

Multi-stage creep tests were performed on the same double-crack specimens using a single-specimen stepwise loading method to avoid the influence of natural variability. The stress levels were set to 50%, 60%, 70%, 80%, 85%, 90% and 95% of the UCS determined from the compression tests. Each stress level was maintained for 8 h, which was sufficient to reach a steady-state creep stage. The loading rate between stages was 0.2 kN/s.

Figure 6 shows the axial creep curves for specimens with crack 2 angles of 30°, 60° and 90° under stepwise loading. At lower stress levels (e.g., 50–70% UCS), only decelerating and steady-state creep were observed. At higher stress levels (≥80% UCS), all three creep stages (decelerating, steady-state and accelerating) were clearly identifiable. The time to failure decreased significantly as the stress level increased. For example, for the specimen with 60° of crack 2, the failure time was 122.2 h at 80% UCS, but only 0.2 h at 95% UCS.

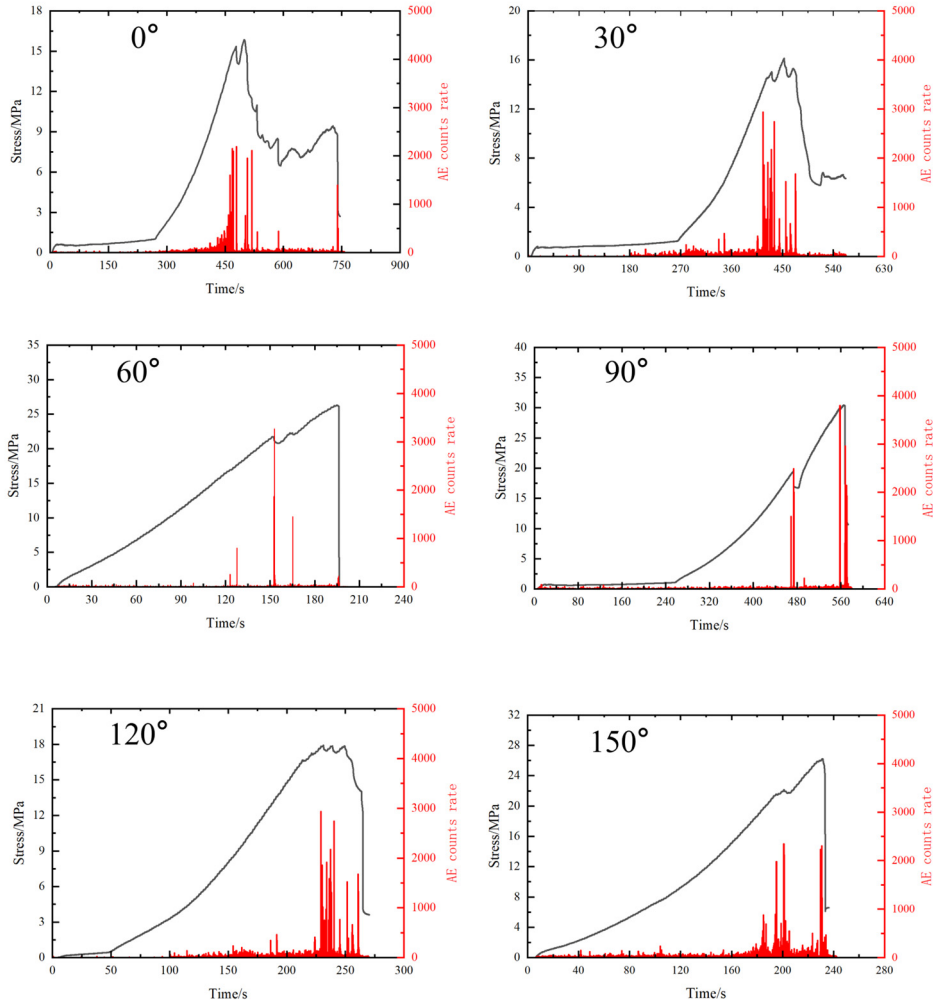


Figure 5. AE ringing count and cumulative energy for selected specimens.

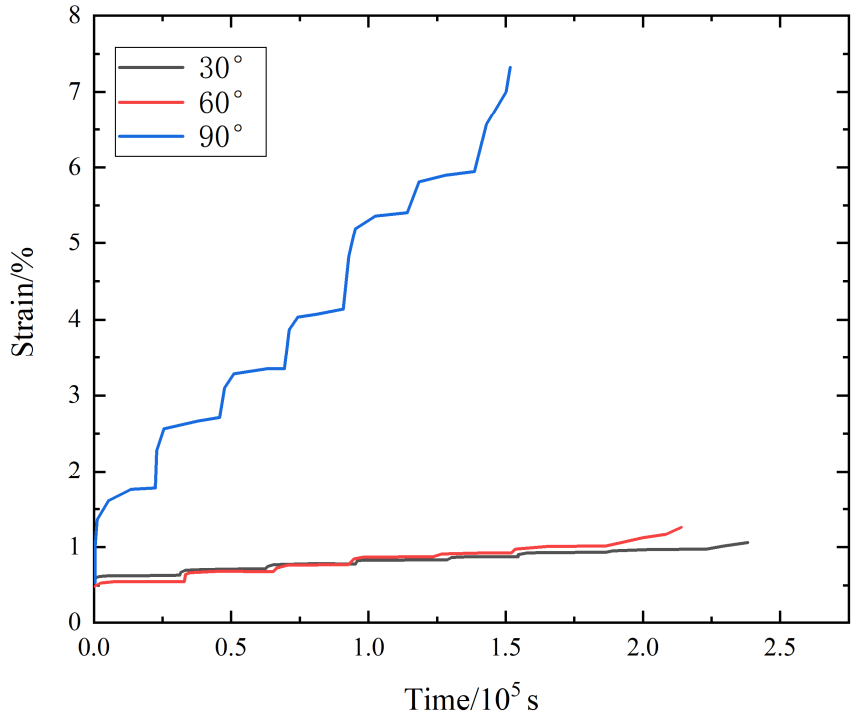
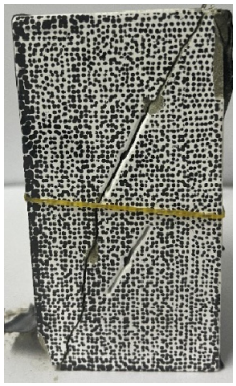
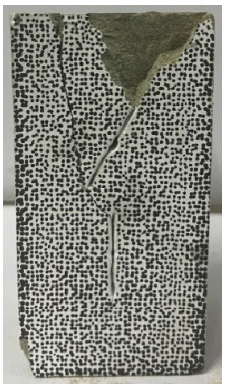


Figure 6. Multi-stage creep curves for double-crack specimens.

The failure patterns under creep loading were similar to those under monotonic compression, with wing cracks initiating from the crack tips and eventually coalescing to form a through-going failure surface. No significant difference in failure mode was observed between creep and monotonic loading (shown in Table 1).

Table 1. Comparison of failure patterns under uniaxial loading and creep loading.

Loading Type	30°	60°	90°
Uniaxial loading			
Creep loading			

3. Numerical Modeling

3.1. UDEC-Voronoi Model Setup

A two-dimensional Voronoi grain-based model was constructed using UDEC 7.0. The model dimensions were 50 mm (width) × 100 mm (height) in Figure 7, matching the laboratory specimens. The bottom boundary is fixed in the y direction, the top boundary moves downwards at a constant velocity v_0 corresponding to an axial loading rate of 0.2 kN/s, the two lateral boundaries are laterally confined, and displacements are constrained in the out-of-plane direction to enforce plane strain. The Voronoi polygons were generated using a built-in statistical algorithm to mimic the grain size distribution of the actual sandstone, with equivalent grain diameters ranging from approximately 0.7 mm near the central to 1.6 mm near the boundaries. The total number of Voronoi blocks was approximately 3200. A plane strain condition was assumed by constraining displacements in the out-of-plane direction. Double pre-existing cracks of the same geometries as in the laboratory were inserted by removing the contacts along the prescribed crack surfaces.

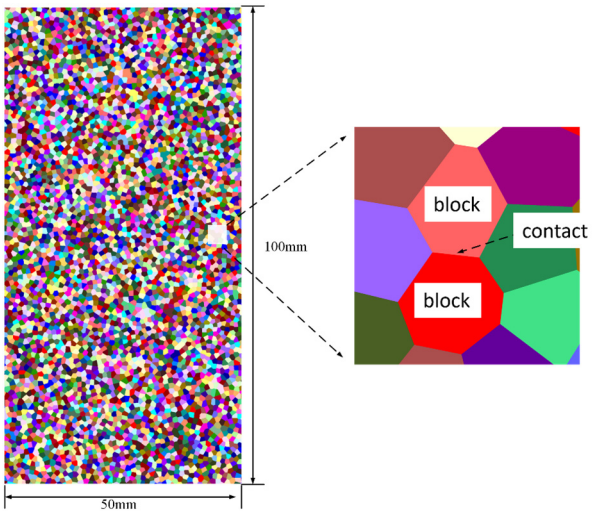


Figure 7. Numerical model with Voronoi blocks.

3.2. Constitutive Model and Calibration

The Voronoi blocks were treated as deformable bodies with a linear elastic constitutive model. The contacts between blocks were governed by the Coulomb slip model with a tension cut-off. The tensile and shear failure of the sub-interfaces is determined by the maximum tensile stress criterion and the Mohr-Coulomb criterion. Once the stress on the contact interface reaches the strength threshold, the interface will fail, leading to fractional slip, tensile damage (opening), or compressive plasticity (overlapping) between the blocks as shown in Figure 8.

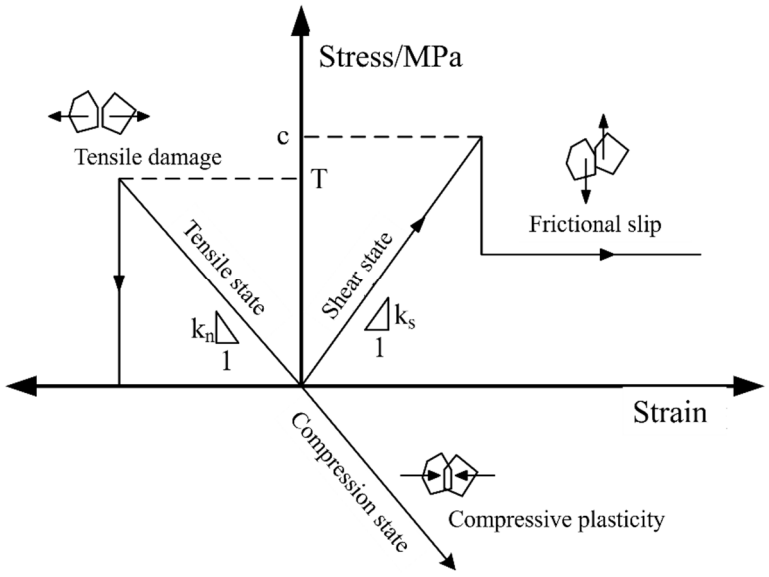


Figure 8. Strength criterion for contacts.

The normal stress increment on the contact interface is:

$$\Delta\sigma_n = -K_n \cdot \Delta U^n \quad (1)$$

where K_n is the normal stiffness of the contact interface (Pa/m), and ΔU^n is the normal displacement increment on the contact interface (m).

The tangential stress vector increment on the contact interface is:

$$\Delta\tau_i^s = -K_s \cdot \Delta U_i^s \quad (2)$$

where K_s is the shear stiffness of the contact interface (Pa/m), and ΔU_i^s is the tangential displacement vector increment on the contact interface (m).

The tensile stress threshold of the contact interface is:

$$J_{Tmax} = -J_T \tag{3}$$

where J_T is the tensile strength of the contact interface (MPa). In UDEC, compressive force is taken as positive. The maximum shear stress on the sub-interface is:

$$\tau_{max}^s = c + \sigma^n \tan\phi \tag{4}$$

where c and ϕ are the cohesion and friction angle of the contact interface, respectively. If the stress on the contact interface exceeds the stress threshold, the tensile strength or cohesion is set to zero:

$$\begin{aligned} &\text{For tensile damage in tensile state, if } \sigma^n < J_{T\max}, \text{ then } \sigma_n = 0, \tau_i^s = 0. \\ &\text{For fractional slip in shear state, if } \tau^s > \tau_{\max}^s, \text{ then } \tau_i^s = \tau_i^0 \sigma^n \tan\varphi. \end{aligned}$$

where τ_i^0 is the unit tangential stress vector.

Rock is a polycrystalline material formed by cementation of various mineral crystals under specific environmental conditions (in situ stress, groundwater, temperature, etc.) and contains micro-defects such as microcracks and pores. At the meso-scale, the deformation and fracture process of rock is essentially the evolution of internal microcrack initiation, propagation, and coalescence. Under loading, an equivalent local tensile stress field develops around microcracks or pores inside the rock. When the stress intensity factor K_I at the crack tip reaches the fracture toughness K_{IC}, the crack propagates instantaneously at sonic speed. If K_I is below K_{IC} but higher than the lower limit K_0 of the stress intensity factor, stable slow crack growth occurs at the crack tip. The crack length gradually increases to a critical length, causing K_I to eventually reach K_{IC}, and then the crack propagates instantaneously. This phenomenon is known as subcritical crack growth. Subcritical crack growth is an important mechanism explaining time-dependent deformation and failure of rock at the meso-scale. Among these, stress corrosion is considered the dominant factor driving time-dependent deformation of rock. Charles [23] first studied the static fatigue fracture process of soda-lime glass under tensile loading, analyzed its sensitivity to water vapor corrosion, described the relationship between subcritical crack growth velocity and stress intensity factor under the combined action of stress and water (commonly referred to as stress corrosion), and proposed the widely used subcritical crack growth equation:

$$v = v_0 \exp(-\Delta H/RT) K_I^n \tag{5}$$

where v is the microcrack growth rate; v_0 is the pre-exponential factor; ΔH is the activation enthalpy; R is the universal gas constant; T is the absolute temperature; n is the stress corrosion index; and K_I is the mode I (opening mode) stress intensity factor.

Furthermore, based on chemical reaction rate theory, researchers proposed that the corrosion reaction at the crack tip in soda-lime glass is a chemical activation process between glass and water with stress-dependent activation energy, and the reaction rate is strongly influenced by the OH^- ion concentration at the crack tip. They derived an equation for crack propagation under the influence of water environment and crack-tip stress:

$$v = v_0 \exp\left(\frac{v^+\sigma - \left(E^+(0) + c\sigma^2 + v_M\zeta/2r\right)}{RT}\right) \tag{6}$$

where v^+ is the activation volume; σ is the tensile stress at the crack tip; $E^+(0)$ is the activation energy without stress influence; v_M is the molar volume of glass; ζ is the interfacial surface energy between glass and reaction products; ρ is the radius of curvature at the crack tip;

and $c\sigma^2$ accounts for the combined effect of strain energy loss due to corrosion and the second-order expansion term of activation energy. The terms γ and σ^2 are very small compared to other terms in the equation and can be neglected; thus, the above equation is simplified to:

$$v = v_o \exp\left(-\frac{E^+(0) - v^+\sigma}{RT}\right) \quad (7)$$

The stress corrosion theory described above is introduced into the Voronoi polygon-based discrete element model to establish a meso-scale time-dependent deformation numerical model of sandstone specimens. In the model, Voronoi polygons of various shapes and sizes are bonded together to form the numerical sandstone specimen. We assume that stress corrosion reactions occur only on the contacts between polygons and do not alter the mechanical properties of the polygons themselves. Each contact is a potential corrosion reaction zone, and any resulting microcracks propagate only along the contacts between polygons. Under sustained loading, the meso-scale time-dependent deformation process of the numerical sandstone specimen is essentially a process in which stress corrosion reactions progressively weaken the cohesion and tensile strength of the contacts, as illustrated in Figure 9. The rate of weakening of cohesion and tensile strength on a contact is proportional to the chemical reaction rate. This assumption is similar to the parallel-bonded stress corrosion (PSC) model proposed by Potyondy. The friction angle on a contact is mainly related to its roughness and has little effect on the strength degradation of the sub-contact. Therefore, we assume that the friction angle is independent of the time-dependent degradation of mechanical strength.

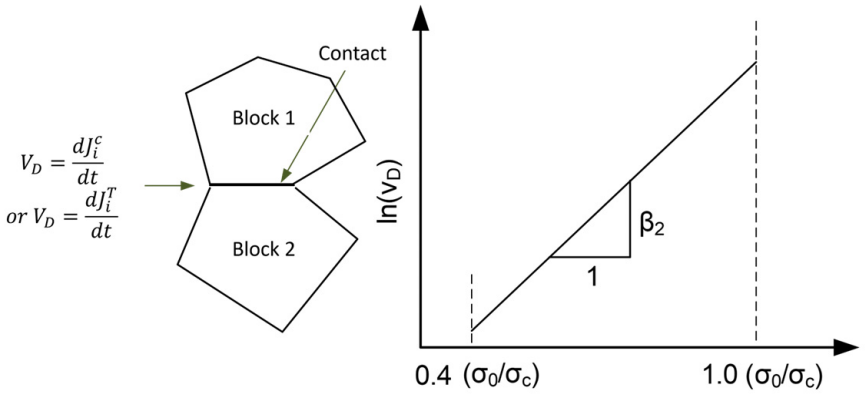


Figure 9. Relationship of the corrosion weakening rate on the contacts in the Voronoi polygon-based discrete element model. σ_0 is the threshold stress (also referred to as the activation stress), stress corrosion reaction does not occur when the stress is below this value, which is approximately 0.4 times of the peak stress of the rock specimen, σ_c is the peak stress of the rock specimen. J_i^T and J_i^c are the tensile strength and cohesion on the i-th sub-contact of the contact interface respectively.

The micro-parameters included the normal stiffness (K_n), shear stiffness (K_s), cohesion (J_c), tensile strength (J_T) and friction angle (ϕ). These parameters cannot be measured directly and were calibrated through a trial-and-error process by matching the numerical stress–strain curve and failure pattern to the laboratory results for intact and pre-existing crack specimens. The calibrated micro-parameters are listed in Table 2. The stress corrosion parameters for creep simulation were set as $\beta_1 = 6.5 \times 10^{-3}$ and $\beta_2 = 2.8 \times 10^{-7}$, following the approach of Potyondy [24,25].

Table 2. Calibrated micro-parameters of the Voronoi grain-based model.

Parameters	Value
Modulus $\boldsymbol{E}$/GPa	9.5
Poisson's ratio $\boldsymbol{\nu}$	0.23
Normal stiffness K_n/GPa/mm	40
K_n/K_s	2
Tensile strength J_T/MPa	26.4
Cohesion J_c/MPa	6.9
Friction angle ϕ/°	27
Residual friction angle ϕr/°	6

4. Results

The fracture modes of double-crack specimens with crack inclination angles of 0°, 30°, 60°, 90°, 120°, and 150° under uniaxial compression are shown in Figure 10. As the pressure at both the upper and lower ends continues to increase, shear microcracks or tensile microcracks within the rock mass propagate and coalesce. These shear or tensile microcracks degrade the internal load-bearing framework of the rock, gradually leading to the formation of macroscopic cracks. After the rock reaches its peak strength, its load-bearing capacity drops significantly, manifested as a sharp decline in the stress curve. Overall, for different crack inclination angles, the final failure mode of the specimens is predominantly tensile failure (generating tensile microcracks), accompanied by localized shear failure (generating shear microcracks).

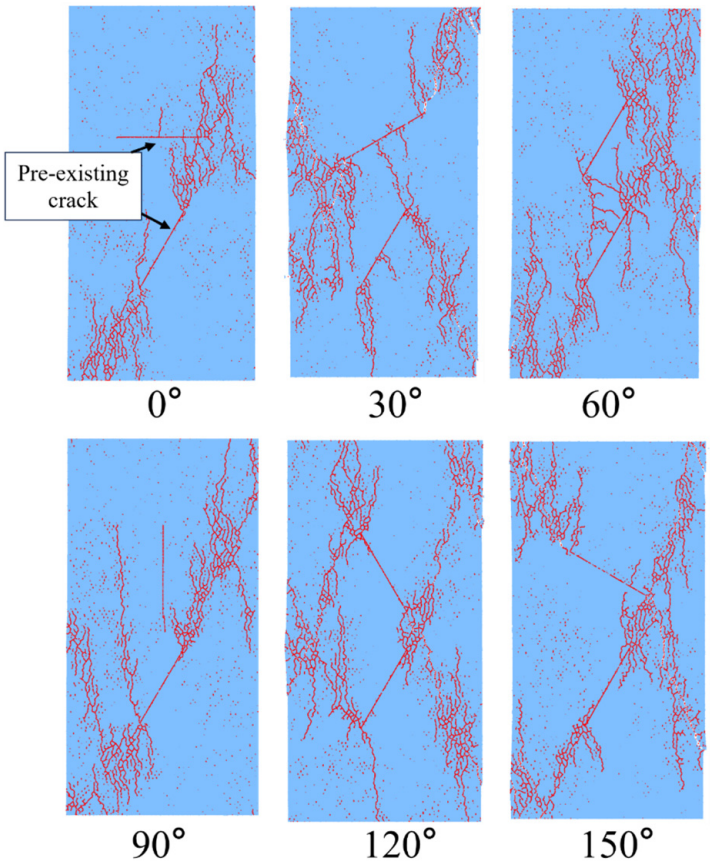


Figure 10. Fracture modes of double-crack specimens with different crack inclination angles under uniaxial loading.

The uniaxial compressive strength curves of double-crack specimens with various crack-2 inclination angles (0°, 30°, 60°, 90°, 120°, and 150°) are shown in Figure 11. The corresponding compressive strengths are 16.6, 17.2, 26.5, 29.1, 21.9, and 28.1 MPa. With increasing crack inclination angle, the compressive strength first decreases, then increases, and decreases again, reaching its minimum at 30°. For all specimens, tensile microcracks significantly outnumber shear microcracks when macroscopic fracture occurs. The simulated UCS values for different crack inclinations are compared with the experimental results in Table 3, showing good agreement.

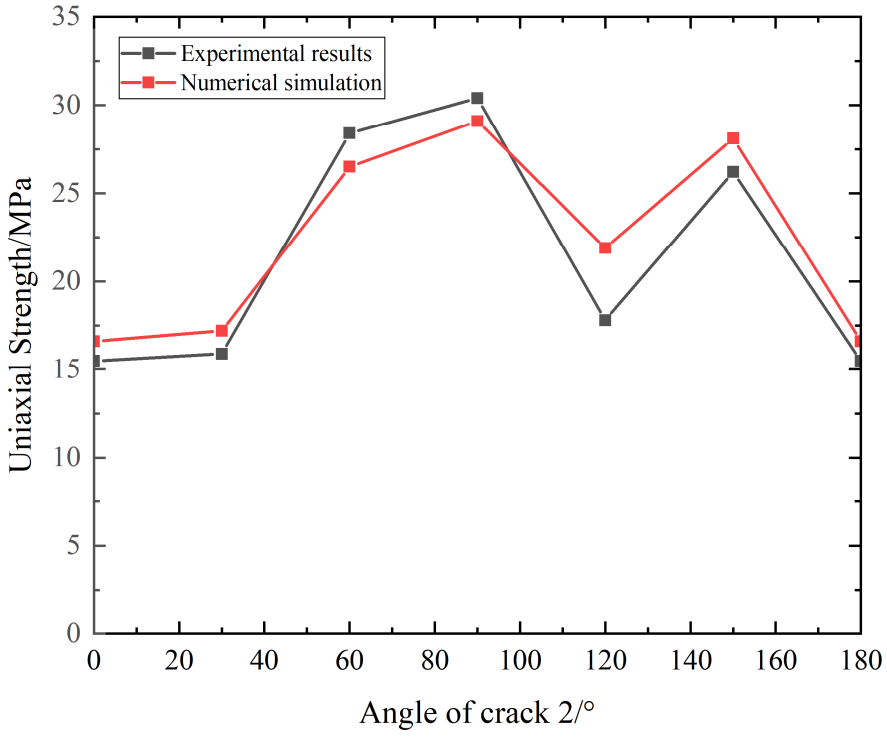


Figure 11. Strength of experimental results and numerical simulation with different crack inclination angles under uniaxial loading.

Table 3. Comparison of experimental and numerical UCS for different crack 2 angles.

Crack 2 Angle (°)	Experimental UCS (MPa)	Numerical UCS (MPa)
Intact	42.4	42.4
0	15.5	16.6
30	15.9	17.2
60	28.4	26.5
90	30.4	29.1
120	17.8	21.9
150	26.2	28.1

Figure 12 shows the creep curves and macroscopic fracture morphologies of double-crack specimens with different inclination angles (0°, 30°, 60°, 90°, 120°, and 150°) under a stress level of 80%. It can be observed from the figure that all specimens exhibit three stages of creep deformation under the same stress level, but the creep rupture times vary without a clear trend. For example, the creep rupture times for specimens with inclination angles of 0°, 30°, and 60° are 69.4, 34.2, and 122.22 h, respectively.

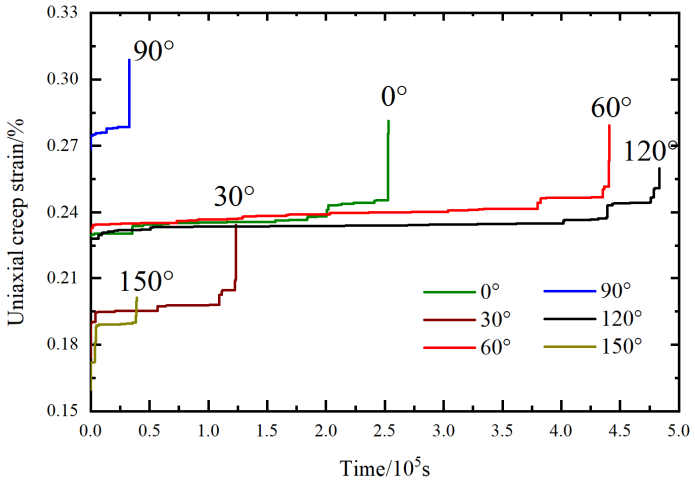


Figure 12. The relationship curves between axial strain and time for double-flaw specimens with different inclination angles under a stress level of 80% σc.

During uniaxial compressive creep, microcracks first initiate and propagate at the tips of the pre-existing cracks. Initially, these microcracks expand steadily along the direction of maximum compressive stress (i.e., the axial direction) and gradually evolve into prominent wing cracks. As the load continues to be applied, the wing cracks further extend toward the ends of the specimen, potentially interacting and coalescing with adjacent cracks, and eventually form a penetrating macroscopic main crack, leading to the destabilization and failure of the specimen (Figure 13).

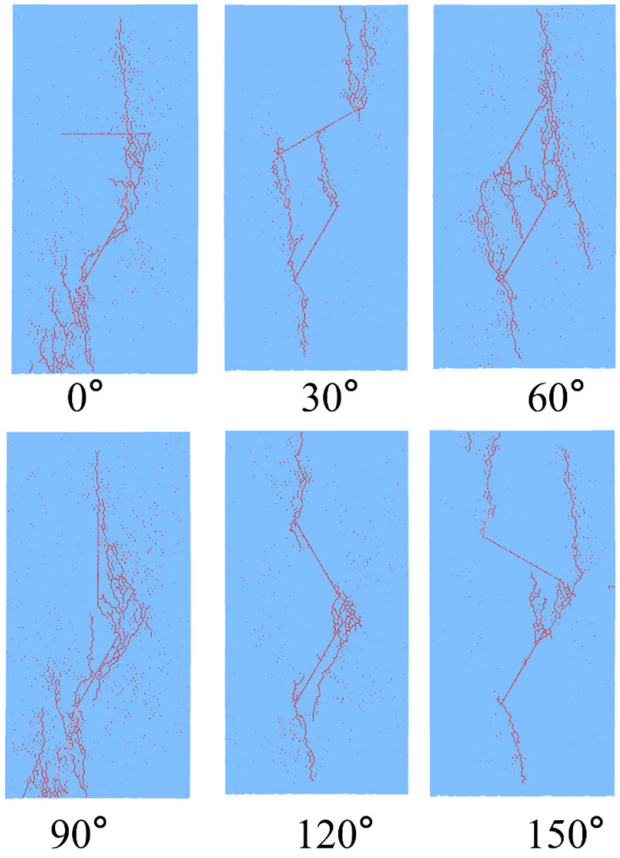


Figure 13. Simulated crack distribution and failure patterns of double-crack specimens with different crack-2 inclination angles under creep loading.

For different crack 2 inclinations under 80% UCS, the simulated creep lifetimes varied: 69.4 h (0°), 34.2 h (30°), 122.2 h (60°), 89.5 h (90°), 45.0 h (120°) and 78.0 h (150°). The 30° inclination exhibited the shortest lifetime, indicating that this geometry is most prone to time-dependent failure.

5. Discussion

5.1. Effect of Crack Inclination on Strength and Failure

The non-linear relationship between crack inclination and UCS observed in both experiments and simulations can be explained by the orientation of the maximum tensile stress concentration at the crack tips. For crack 2 angles of 0° and 30°, the crack is nearly parallel to the loading direction, resulting in high shear stress concentration and early wing crack initiation, leading to low strength. For 60° and 90°, the crack is steeply inclined or vertical, requiring higher axial stress to generate sufficient tensile stress at the tips, thus higher strength. The resurgence of strength at 150° (which is equivalent to 30° but mirrored) suggests that the interaction between the crack 1 and crack 2 also plays a role. The relatively high strength at 150° may be due to the shielding effect of the upper crack.

5.2. Dominance of Tensile Microcracks

Both DIC/AE experiments and numerical simulations confirm that tensile microcracks far outnumber shear microcracks during the entire failure process. This is because sandstone is much weaker in tension than in compression. Even under uniaxial compression, local tensile stresses develop around crack tips and grain boundaries, causing tensile cracking. This finding has important implications for hazard assessment: rock masses with pre-existing fractures are prone to sudden tensile failure, which can be difficult to predict using shear-based criteria.

5.3. Creep Behavior and Stress Corrosion

The three-stage creep behavior observed in the experiments and reproduced by the numerical model with stress corrosion parameters indicates that time-dependent crack growth is controlled by subcritical crack propagation. The acceleration stage occurs when the cumulative microcrack density reaches a critical threshold, leading to rapid coalescence. The strong dependence of creep lifetime on stress level (e.g., from 122 h at 80% UCS to 0.2 h at 95% UCS) suggests that a small increase in stress can drastically reduce the service life of a fractured rock mass. For engineering practice, a conservative design stress of $\leq$70% UCS is recommended to avoid accelerating creep.

There are three reasons for the discrepancies between the experimental and simulated creep curves from the multi-stage creep tests. First, the multi-stage creep tests apply stress as a percentage of the measured UCS, whereas the simulation applies the same percentage of the simulated UCS; since the two UCS values differ by up to 23% (Table 3), the absolute stress levels are not identical, which directly shifts the creep lifetime. Second, the two stress-corrosion parameters ($\beta_1 = 6.5 \times 10^{-3}$, $\beta_2 = 2.8 \times 10^{-7}$) were calibrated against the UCS test, and the remaining cases are predictions. Third, the two-dimensional plane-strain model omits out-of-plane flaw growth and therefore tends to overestimate the lifetime.

5.4. Role of the Rock Bridge in the Failure Process of Double-Crack Specimens and Its Relationship with Crack Inclination Angle

In specimens containing two pre-existing cracks, the unbroken rock region between the two cracks is termed the rock bridge. The coalescence mode of the rock bridge directly determines the macroscopic failure morphology of the specimen and is significantly influenced by the crack inclination angle. Overall, for all inclination angles, the coalescence

of the rock bridge is dominated by tensile coalescence. However, the specific coalescence mechanism of the rock bridge and its contribution to specimen strength vary with crack inclination angle.

When the crack inclination angle is small (0° and 30°), the two cracks are nearly parallel to the loading direction. Under axial compression, wing tensile cracks first initiate at the crack tips, propagate along the direction of maximum compressive stress (axial direction), and quickly traverse the rock bridge region, resulting in brittle coalescence dominated by tension. Because the rock bridge is penetrated at a low stress level, the specimen exhibits a low peak strength (e.g., the minimum strength of 15.9 MPa at 30°). At the later stage of rock bridge coalescence, a small number of shear microcracks also appear due to local shear stress concentration, forming a tensile-shear mixed failure mode, but tensile cracks still dominate overwhelmingly.

When the crack inclination angle increases to 60° and 90°, the cracks are steeply inclined or nearly perpendicular to the rock bridge direction. In this case, wing tensile cracks must overcome greater confining constraints to traverse the rock bridge; therefore, the axial stress required for rock bridge coalescence increases significantly, and the specimen strength becomes higher (reaching 30.4 MPa at 90°). For these inclination angles, the rock bridge failure mode is dominated by pure tensile coalescence, with very few shear cracks and a straighter crack propagation path.

For crack inclination angles of 120° and 150°, the geometric relationship between the upper and lower cracks is mirrored. The rock bridge is located in the overlapping zone of the two cracks, and the upper crack exerts a shielding effect on the lower crack, delaying the propagation of tensile cracks. Consequently, although 150° is geometrically symmetric to 30°, its strength (26.2 MPa) is slightly higher than that at 30°, and rock bridge coalescence is characterized by more deflection and detouring of tensile cracks. It is worth noting that for all inclination angles, rock bridge coalescence is always accompanied by pronounced wing crack development, and the coalescence path is mainly axial, indicating that the direction of maximum compressive stress controls the tensile failure mode of the rock bridge.

In summary, the coalescence of the rock bridge in double-crack specimens is dominated by tensile failure, with shear failure playing only a local auxiliary role. The crack inclination angle regulates the initiation and propagation resistance of tensile cracks by altering the local stress state in the rock bridge region, thereby leading to a non-linear variation of strength. This understanding has important implications for the stability assessment of fractured rock masses: instability in rock masses containing double-crack structures is often triggered by sudden tensile coalescence of the rock bridge, and traditional criteria based on shear sliding may underestimate the failure risk.

The findings highlight that fracture-induced instability is not simply a function of stress magnitude but also of fracture geometry. In deep mining, roof strata containing sub-horizontal (0–30°) or moderately inclined (30–60°) fractures are particularly vulnerable, as they exhibit low strength and short creep lifetimes. Monitoring of fracture orientations using borehole imaging should be prioritized in high-risk areas. Furthermore, the validated UDEC-Voronoi model can serve as a predictive tool for assessing long-term stability under different stress paths and fracture configurations.

5.5. Limitations and Future Work

FEM requires a pre-defined crack path and cannot spontaneously generate wing cracks or bridge coalescence. LEFM provides the stress-intensity framework but assumes a homogeneous medium and a dominant single crack; it therefore cannot capture the interaction between two flaws within a heterogeneous grain assemblage. PFC-PBM reproduces microcracking statistics but uses circular particles, which cannot represent the grain geometry

or the intergranular/transgranular paths of sandstone. Rigid-block discrete models cannot represent deformable grains with time-dependent degradation. We also now state explicitly which concept is used where LEFM-based subcritical crack growth underlies Equations (5)–(7) and the contact degradation law; the Mohr–Coulomb criterion is applied at the sub-contact level (Equation (4)) rather than as a macroscopic strength criterion; and the maximum tensile stress criterion governs tensile failure of contacts (Equation (3)).

The classical strength and failure criteria are assessed as follows. (1) The Mohr–Coulomb criterion contains no information on crack orientation and therefore predicts identical strengths for the 30° and 90° configurations. Our measured strengths (15.9 MPa vs. 30.4 MPa, Table 3) contradict its use as an isotropic criterion; it can be retained only if the cohesion and friction angle are made orientation-dependent, which removes its predictive value. (2) The Hoek–Brown criterion describes jointed rock masses through the empirical constant m_i and cannot resolve the relative orientation of two discrete cracks; our data therefore fall outside its scope. (3) A maximum tensile stress/stress-concentration criterion is confirmed: the nonlinear UCS–inclination relationship follows directly from the tensile stress concentration at the crack tips (Figures 3 and 11), and the tensile-dominated microcracking (>90%) supports it.

Finally, several limitations of this study should be acknowledged. (1) The numerical model is two-dimensional and in plane strain, so out-of-plane crack growth and the three-dimensional geometry of the rock bridge are not represented; this tends to overestimate the creep lifetime. A three-dimensional grain-based model is a priority for future work. (2) The pre-existing cracks are idealized as straight, through-thickness slots, whereas natural fractures are rough, branched, and sometimes mineral-filled; reconstructing real flaw geometries from CT data would improve realism. (3) Only one lithology (red sandstone), one specimen size (50 × 50 × 100 mm), and one batch were tested, so the scale effect and batch-to-batch variability remain to be quantified.

6. Conclusions

This study integrates laboratory experiments and UDEC-Voronoi numerical modeling to investigate the mechanical behavior and failure characteristics of double-pre-cracked sandstone under uniaxial compression and creep conditions. The uniaxial compressive strength of double-crack sandstone depends non-linearly on the inclination angle of the crack 2. Relative to the intact strength of 42.4 MPa, the minimum strength (15.9 MPa) occurs at 30°, and the maximum (30.4 MPa) at 90°. Tensile microcracks dominate the entire failure process, accounting for over 90% of all microcracks, as consistently confirmed by DIC/AE monitoring and numerical simulations; shear microcracks play only a secondary role. Under multi-stage creep loading, the creep lifetime decreases sharply with increasing stress level. For the specimen with a crack inclination of 60°, the time to failure is 122.2 h at 80% of UCS, but only 0.2 h at 95% of UCS, and the creep curves display three distinct stages: decelerating, steady-state, and accelerating creep. The UDEC-Voronoi grain-based model, calibrated against experimental data, successfully reproduces the observed strength anisotropy, crack evolution, and time-dependent deformation, with the simulated accumulation of microcracks following the same three-phase pattern as the laboratory creep strain. From a geohazard perspective, fracture configurations with low (0–30°) or moderate (60°) inclinations are most susceptible to failure under both short-term and long-term loading. Therefore, in deep fractured rock masses, engineering design should account for both the orientation of pre-existing fractures and the stress level to mitigate time-dependent instability.

https://doi.org/10.3390/app162110759

Author Contributions: Y.Y.: data curation, methodology, investigation, formal analysis, writing—original draft; T.-F.F.: formal analysis, software, writing—review and editing; T.-T.C.: methodology, formal analysis, resources, project administration, writing—review and editing; S.-N.Z.: writing—review and editing; L.-K.X.: investigation, methodology. All authors have read and agreed to the published version of the manuscript.

Funding: This research was funded by Innovation and Development Project of Information Institution of Ministry of Emergency Management (2023501 and 2024501) and Key Science and Technology Project of Ministry of Emergency Management of the People's Republic of China (No. 2024EMST080801).

Data Availability Statement: The data that support the findings of this study are available upon request.

Acknowledgments: We would like to acknowledge joint support from Innovation and Development Project of Information Institution of Ministry of Emergency Management (2023501 and 2024501) and Key Science and Technology Project of Ministry of Emergency Management of the People's Republic of China (No. 2024EMST080801).

Conflicts of Interest: The authors declare that they have no known competing financial interests or personal relationships that could have appeared to influence the work reported in this paper.

References

1. Healy, D.; Rizzo, R.; Cornwell, D.; Farrell, N.; Watkins, H.; Timms, N.; Gomez-Rivas, E.; Smith, M. FracPaQ: A MATLAB™ toolbox for the quantification of fracture patterns. *J. Struct. Geol.* **2017**, *95*, 1–16. [CrossRef]
2. Atkinson, B.K. Subcritical crack growth in geological materials. *J. Geophys. Res. Solid Earth* **1984**, *89*, 4077–4114. [CrossRef]
3. Meng, Z.; Zhang, J.; Wang, R. In-situ stress, pore pressure and stress-dependent permeability in the Southern Qinshui Basin. *Int. J. Rock Mech. Min. Sci.* **2011**, *48*, 122–131. [CrossRef]
4. Ranjith, P.G.; Zhao, J.; Ju, M.; De Silva, R.V.; Rathnaweera, T.D.; Bandara, A.K. Opportunities and challenges in deep mining: A brief review. *Engineering* **2017**, *3*, 546–551. [CrossRef]
5. He, M.; Wu, Y.; Gao, Y.; Tao, Z. Research progress of rock mechanics in deep mining. *J. China Coal Soc.* **2024**, *49*, 75–99. [CrossRef]
6. Yuan, Y.; Xu, T.; Meredith, P.G.; Mitchell, T.M.; Heap, M.J.; Heng, Z. A time-dependent microplane model for deformation and fracturing of brittle rock. *Comput. Geotech.* **2025**, *184*, 107278. [CrossRef]
7. He, J.; Lin, C.; Li, X.; Zhang, Y.; Chen, Y. Initiation, propagation, closure and morphology of hydraulic fractures in sandstone cores. *Fuel* **2017**, *208*, 65–70. [CrossRef]
8. Liu, Z.; Chen, M.; Zhang, G. Analysis of the influence of a natural fracture network on hydraulic fracture propagation in carbonate formations. *Rock Mech. Rock Eng.* **2014**, *47*, 575–587. [CrossRef]
9. Zhang, X.; Lu, Y.; Tang, J.; Zhou, Z.; Liao, Y. Experimental study on fracture initiation and propagation in shale using supercritical carbon dioxide fracturing. *Fuel* **2017**, *190*, 370–378. [CrossRef]
10. Yang, D.; Chanchole, S.; Valli, P. Study of the Anisotropic Properties of Argillite Under Moisture and Mechanical Loads. *Rock Mech. Rock Eng.* **2013**, *46*, 247–257. [CrossRef]
11. Wang, W.; Ye, Y.; Wang, Q.; Hu, N. Experimental Study on Anisotropy of Strength, Deformation and Damage Evolution of Contact Zone Composite Rock with DIC and AE Techniques. *Rock Mech. Rock Eng.* **2022**, *55*, 837–853. [CrossRef]
12. Kharghani, M.; Goshtasbi, K.; Nikkhah, M.; Ahangari, K. Investigation of the Kaiser effect in anisotropic rocks with different angles by acoustic emission method. *Appl. Acoust.* **2021**, *175*, 107831. [CrossRef]
13. Heap, M.J.; Brantut, N.; Baud, P.; Meredith, P.G. Time-dependent compaction band formation in sandstone. *J. Geophys. Res. Solid Earth* **2015**, *120*, 4808–4830. [CrossRef]
14. Wang, C.; You, R.; Lv, W.; Sui, Q.; Yan, Y.; Zhu, H. Damage evolution and acoustic emission characteristics of sandstone under freeze–thaw cycles. *Acs Omega* **2024**, *9*, 4892. [CrossRef]
15. Xu, W.; Cao, P. Fracture behaviour of cemented tailing backfill with pre-existing crack and thermal treatment under three-point bending loading: Experimental studies and particle flow code simulation. *Eng. Fract. Mech.* **2018**, *195*, 129–141. [CrossRef]
16. Zhou, Z.; Zhao, Y.; Bi, J.; Cheng, H.; Wang, C. Shear mechanical properties and failure modes of rock with V-shaped intersecting double-cracks. *Theor. Appl. Fract. Mech.* **2023**, *124*, 103755. [CrossRef]
17. Hu, X.; Huang, S.; Yu, S.; Li, Y.; Dong, J. Investigations on the fracture mechanisms of Z-shaped fissured rock-like specimens. *Theor. Appl. Fract. Mech.* **2024**, *134*, 104748. [CrossRef]
18. Scholtès, L.; Donzé, F.-V. A DEM model for soft and hard rocks: Role of grain interlocking on strength. *J. Mech. Phys. Solids* **2013**, *61*, 352–369. [CrossRef]

19. Yang, W.-M.; Geng, Y.; Zhou, Z.-Q.; Li, L.-P.; Gao, C.-L.; Wang, M.-X.; Zhang, D.-S. DEM numerical simulation study on fracture propagation of synchronous fracturing in a double fracture rock mass. *Geomech. Geophys. Geo-Energy Geo-Resour.* **2020**, *6*, 39. [CrossRef]
20. Bai, Q.-S.; Tu, S.-H.; Zhang, C. DEM investigation of the fracture mechanism of rock disc containing hole (s) and its influence on tensile strength. *Theor. Appl. Fract. Mech.* **2016**, *86*, 197–216. [CrossRef]
21. Gui, Y.; Zhao, Z.; Ji, J.; Wang, X.; Zhou, K.; Ma, S. The grain effect of intact rock modelling using discrete element method with Voronoi grains. *Géotechnique Lett.* **2016**, *6*, 136–143. [CrossRef]
22. Li, J.; Konietzky, H.; Frühwirt, T. Voronoi-based DEM simulation approach for sandstone considering grain structure and pore size. *Rock Mech. Rock Eng.* **2017**, *50*, 2749–2761. [CrossRef]
23. Charles, R. Static Fatigue of Glass. *J. Appl. Phys.* **1958**, *29*, 1554–1560. [CrossRef]
24. Fu, T.-F.; Xu, T.; Meredith, P.G.; Mitchell, T.M.; Heap, M.J.; Nara, Y. A meso-mechanical approach to time-dependent deformation and fracturing of partially saturated sandstone. *Int. J. Rock Mech. Min. Sci.* **2021**, *145*, 104840. [CrossRef]
25. Fu, T.-F.; Yan, F.-Y.; Zhu, D.-F.; Li, Y.-T. An internal-strain loading approach for quasi-static fracturing in brittle rocks via the grain-based model. *Eng. Anal. Bound. Elem.* **2024**, *169*, 105996. [CrossRef]

Disclaimer/Publisher's Note: The statements, opinions and data contained in all publications are solely those of the individual author(s) and contributor(s) and not of MDPI and/or the editor(s). MDPI and/or the editor(s) disclaim responsibility for any injury to people or property resulting from any ideas, methods, instructions or products referred to in the content.